Multi-Stage Phase-Segregation of Mixed Halide Perovskites under Illumination: A Quantitative Comparison of Experimental Observations and Thermodynamic Models

Klara Suchan, Justus Just, Pascal Beblo, Carolin Rehermann, Aboma Merdasa, Roland Mainz,* Ivan G. Scheblykin,* and Eva Unger*

Photo- and charge-carrier-induced ion migration is a major challenge when utilizing metal halide perovskite semiconductors for optoelectronic applications. For mixed iodide/bromide perovskites, the compositional instability due to light- or electrical bias induced phase-segregation restricts the exploitation of the entire bandgap range. Previous experimental and theoretical work suggests that excited states or charge carriers trigger the process, but the exact mechanism is still under debate. To identify the mechanism and cause of light-induced phase-segregation phenomena, the full compositional range of methylammonium lead bromide/iodide samples are investigated, $MAPb(Br_xI_{1-x})_3$ with $x = 0...1$, by simultaneous in situ X-ray diffraction (XRD) and photoluminescence (PL) spectroscopy during illumination. The quantitative comparison of composition-dependent in situ XRD and PL shows that at excitation densities of 1 sun, only the initial stage of photo-segregation is rationalized with the previously established thermodynamic models. However, a progression of the phase segregation is observed that is rationalized by considering long-lived accumulative photo-induced material alterations. It is suggested that (additional) photo-induced defects, possibly halide vacancies and interstitials, need to be considered to fully rationalize light-induced phase segregation and anticipate the findings to provide crucial insight for the development of more sophisticated models.

1. Introduction

The seamless bandgap tunability of metal halide perovskites (MHPs) with the structure ABX_3 makes these semiconductors an interesting absorber and emitter material for optoelectronic devices like solar cells and light-emitting devices (LEDs). Compositional stability is a prerequisite for both the color stability of LED devices, as well as for stable, reliable, and highly efficient solar cells. Halide mixing/alloying to $X = (I, Br)$ or $X = (Br, Cl)$ has been a common strategy to tune the MHP bandgap. However, this strategy is limited by the light-induced formation of low-bandgap phases for samples with bromide fractions of $x > 0.17$.[1–9] Here, the emission energy is observed to red-shift during illumination due to charge-carrier funneling into the new low bandgap regions.[1] In LED devices this leads to color instability of the emitted light. In solar cells with A = MA, MAFA, or MAFACs with $x > 0.3$, the device efficiency has been shown to drop significantly, likely a result of

K. Suchan, I. G. Scheblykin, E. Unger
Division of Chemical Physics and NanoLund
Lund University
PO Box 124, 22100 Lund, Sweden
E-mail: ivan.scheblykin@chemphys.lu.se
J. Just
MAX IV Laboratory
Lund University
PO Box 118, 22100 Lund, Sweden

P. Beblo
Structure and Dynamics of Energy Materials
Helmholtz-Zentrum Berlin für Materialien und Energie GmbH
Hahn-Meitner-Platz 1, 14109 Berlin, Germany
P. Beblo, R. Mainz
Microstructure and Residual Stress Analysis
Helmholtz-Zentrum Berlin für Materialien und Energie GmbH
Albert-Einstein-Straße 15, 12489 Berlin, Germany
E-mail: roland.mainz@helmholtz-berlin.de
C. Rehermann, A. Merdasa, E. Unger
Department Solution-Processing of Hybrid Materials and Devices
Helmholtz-Zentrum Berlin für Materialien und Energie GmbH
Kekuléstraße 5, 12489 Berlin, Germany
E-mail: eva.unger@helmholtz-berlin.de
C. Rehermann, E. Unger
Research Group Hybrid Materials: Formation and Scaling
Humboldt Universität zu Berlin
IRIS Adlershof
Am Großen Windkanal 2, 12489 Berlin, Germany

charge-carrier trapping in I-rich domains and fermi-level pinning.[10–13] An in-depth understanding of the photo-segregation mechanism and how the process is affected by the bromide/iodide ratio is therefore of paramount importance to evaluate the operational stability and performance limits of MHP-based optoelectronic devices. In this work, we analyze the compositional dependence of photo-segregation to gain new insights into the role of local bandgap variations and inhomogeneous charge-carrier distributions in photo-segregation.

Numerous photoluminescence (PL) measurements on MAPb($I_{1-x}Br_x$)$_3$, showed that the PL peak emission red-shifts upon illumination to ≈1.7 eV, equivalent to a MAPb($I_{1-x}Br_x$)$_3$ composition between x = 0.15–0.2, for all compositions with x > 0.17.[1–7,9,14] Even for different cations and mixtures thereof, low-energy PL peaks corresponding to similar compositions have been shown to evolve.[3] The similarity in the peak energy of evolving PL spectra irrespective of the sample's composition, led to the hypothesis of the existence of thermodynamically-favored compositions adopted by the material upon phase-segregation.[1,4,15–19] This gave rise to the notion, that the photo-segregation process is nearly independent of the sample composition.[20,21] However, this notion is based on PL data, which is prone to probe the lowest accessible low energy emissive states in the sample.

X-ray diffraction (XRD) or optical absorption measurements have been used to investigate the compositional changes in mixed halide samples upon illumination.[1–3,14,22–28] These studies have, however, often only been carried out on samples in a narrow compositional range, with a focus on compositions between x = 0.4 and x = 0.6. Early XRD measurements showed the establishment of an I-rich minority phase (x = 0.2) and a Br-rich majority (x = 0.7) phase under illumination. Subsequent measurements failed to reproduce the result.[1,14,23–27] So far no agreement on evolution of structural properties upon illumination has been reached.[3]

While light-[1–3,6,7,22] bias-[27,29] and electron-beam induced phase-segregation[30,31] are shown to result from ion migration, highlighting the remarkable ion mobility in MHPs, the exact mechanism causing the ions to segregate is still under debate. Due to the reversibility of photo-segregation, it has been postulated to be a charge-carrier-induced transient state.[1–3] Brennen et al. compared and contrasted the models and categorized them into three categories:[3] The first category is based on the generation of an electric field induced by charge-carrier segregation or a gradient in the generation rate causing ions to drift.[32,33] For these effects to cause phase-segregation, a difference in the ionic mobility of bromide and iodide is a prerequisite. A second category of models postulated the formation of polarons[15,17,34] inducing local lattice strain and attracting or repelling certain charge-carriers. While some experimental observation could be rationalized, these models fall short, e.g., in rationalizing the reported excitation density threshold of the photo-segregation.[7,35] This is accounted for in a third class of models, referred to as charge carrier localization models, triggered by the energy gain of photo-carriers when funneling into spontaneously formed low-bandgap domains.[7,19,36] What is yet not clear, and what will be further discussed herein, is how charge carrier localization leads to subsequent stabilization and growth of low-energy domains

and how this causes changes in the phase-distribution in the entire sample.

To assess the validity of different models derived to describe the photo-segregation, this study investigated the steady-state phase-distribution of MAPb(Br_xI_{1-x})$_3$ samples under illumination. For the polaron model, it was postulated, that mixed bromide/iodide samples should favorably segregate into phase-distributions dominantly centered around the compositions of x = 0.2 and x = 0.8 when illuminated, which would be consistent with the observation of an emissive state during PL measurements around x = 0.2.[15,17,18,37] The charge-carrier localization model, however, does not predict thermodynamically-preferred compositions despite the pure perovskites but predicts the favorable formation of low-energy states through which charge-carriers recombine as this stabilizes the excited state. This model hence contradicts the hypothesis, that the mixed bromide/iodide perovskite should be prone to segregate into specific phases, e.g., with x = 0.8 and x = 0.2 independent of the bulk material composition.[37] What has to be noted is that these thermodynamic calculations only consider the initial stage of phase-segregation in which initial I-rich nano-domains are formed. In contrast to this, experiments show substantial fractions of the material in a phase-segregated state.[1,7,22]

We therefore set out to test existing hypotheses and models to see whether they are sufficient to describe all stages of phase-segregation observed experimentally. To probe both, the evolution of low-energy emitting sites and the overall phase-distribution of the samples, we studied the photo-induced phase-segregation in MAPb(Br_xI_{1-x})$_3$ samples correlatively with PL and XRD across the entire compositional range. For this, we built a setup, shown in **Figure 1**, allowing us to keep samples in an inert environment, with a blue LED light-source for illumination at an equivalent of 1 sun enabling the simultaneous measurements of X-ray diffraction (XRD) and Photoluminescence (PL). This provided a dataset that allows us to compare the equilibrium phase-distribution for MAPb(Br_xI_{1-x})$_3$ samples in the dark and light quantitatively and study the phase-segregation kinetics as a function of composition.

We observe that X-ray diffraction patterns adopted in equilibrium under illumination are highly dependent on the sample composition. The phase-distribution appears to be asymmetric and compositions with opposite bromide:iodide are not *mirror-images*. This indicates that the photo-segregation process does not affect bromide and iodide in the same manner. We derive and quantify the distribution of compositional phases as the degree of segregation and evaluate the quantitative evolution of the phase-distribution change through this parameter, in situ, during phase-segregation. The obtained phase-distribution can directly be used to calculate the energy difference between the mixed and the segregated state, giving an estimate of the thermodynamic stability. The comparison with theoretical predictions, discussed in detail in Section 3.2, yields, that at moderate charge-carrier densities, as used in this study, the average charge-carrier energy is not sufficient to rationalize the magnitude of changes in the phase-distributions observed. This means that the initially formed segregated domains are unstable against mixing because the light intensity is too low to sustain them. To reconcile the discrepancy between the thermodynamic models and the experimentally observed segregated state, we postulate
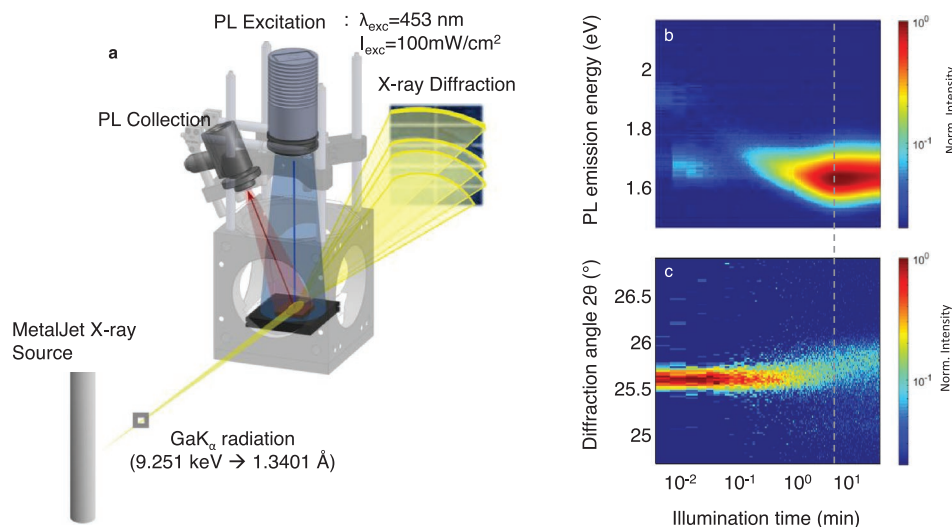
Figure 1. a) Schematic drawing of the atmosphere and temperature-controlled measurement set-up developed to study the change in the structural and optical properties of $MAPb(Br_xI_{1-x})_3$ simultaneously during illumination. b) PL spectra of a sample with $\overline{x} = 0.6$ during illumination. The color represents the luminescence intensity. c) XRD patterns of the 200 reflex of the same sample during illumination, here the color represents the scattering intensity. Please note the log scale of the time and intensity.

that light-induced effects in the material, such as photo-induced formation of iodide vacancies and interstitials, accumulate over time. This effectively makes the rates of the mixing and de-mixing processes different which is a pre-requisite for the kinetic model suggested by Kuno et al.[3] As a result, the phase-segregation is feasible even at moderate light intensities, by making the segregation process more efficient than the mixing process. In line with the experimentally observed apparent higher mobility of iodide compared to bromide ions, we postulate that preferential iodide-oxidation and lead-iodide bond cleavage causing iodide vacancies and interstitials,[38–41] is an effect that becomes greatly enhanced, when charge-carriers accumulated on iodide-rich domains causing dramatically-enhanced local charge carrier densities. We propose, that in the derivation of more refined theoretical models, both, thermodynamic driving forces as well as the effect of accumulative photo-induced changes in the material need to be considered.
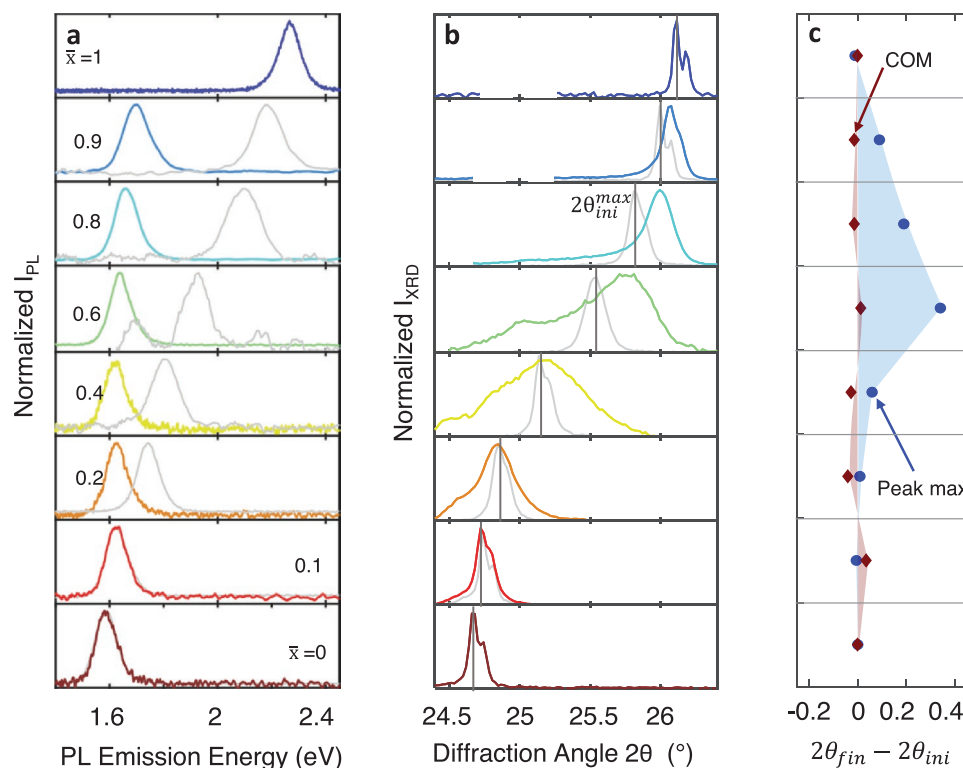
2. Results

2.1. Equilibrium States

In **Figure 2**a, PL spectra and XRD patterns of the initial and final state for the samples of $MAPb(Br_xI_{1-x})_3$ with $\overline{x} = 0, 0.1, 0.2, 0.4, 0.6, 0.8, 0.9, 1$ are compared. The initial XRD patterns are taken prior to illumination with an integration time of 2.5 min, to ensure high accuracy. For PL, the first spectrum is taken for each sample. As the integration time of PL was set to 100 ms or 500 ms, depending on the sample, the gained information is an average over the first 100 or 500 ms respectively. The final PL spectra and XRD pattern are taken when both PL and XRD no longer change. The static nature of the signals in the equilibrium stage allowed for integration over several minutes to achieve a sufficient signal to noise ratio.

The initial PL spectra, as well as XRD patterns in the dark are consistent with literature data from the expected compositions[21,42,43] (see Figure S8, Supporting Information). We therefore conclude that the average sample composition $\overline{x}$ is similar to the halide-ratio of the precursor solution, meaning that no halide is lost during preparation. Further, the initial broadening of the XRD patterns is overall at the lower end of previously reported peaks widths. (Figure S18, Supporting Information). We therefore conclude that in the very beginning of illumination, samples are in a mixed state. However, a slight broadening of the FWHM of the XRD peaks is observed for compositions close to the 50/50 mixture indicating increased inhomogeneity, in agreement with previous reports and further discussed in SI Note 3.[1,14,43] For the sample with $\overline{x} = 0.6$, the PL peak shifts so quickly, that within the first 500 ms, traces of the low PL peak are already visible in the spectrum.

Upon illumination, the steady state PL peak position shifts to lower energy. After prolonged illumination it is comparable for all mixed halide samples with $\overline{x} > 0.1$[1,4] with a slight shift toward higher energy with increasing Br content. Hence irrespective of the sample's average composition $\overline{x}$, the PL emission occurs from states with a high relative iodide content of $x = 0.1$–0.2. This similarity of the PL peak emission energy has been previously attributed to the formation of low-bandgap, iodide-rich, domains whose composition is largely independent of the bulk composition.[1,2,7,15]

Simultaneously, the XRD peak intensity decreases, and the peaks broaden and shift for all mixed halide samples as apparent from the normalized XRD patterns for the dark and illuminated equilibrium states, $I_{XRD_{ini}}(2\theta)$ and $I_{XRD_{fin}}(2\theta)$, for each $\overline{x}$. In contrast to the PL spectra, XRD-patterns of illuminated samples are characteristically different for samples of different average composition, $\overline{x}$. Pure samples, $\overline{x} = 0$ and $\overline{x} = 1$, exhibit no significant change. Samples with $\overline{x} < 0.5$ exhibit broadened XRD peaks upon illumination whereas samples

**ADVANCED
SCIENCE NEWS**

www.advancedsciencenews.com

**ADVANCED
FUNCTIONAL
MATERIALS**

www.afm-journal.de

Figure 2. a) PL spectra of the mixed state (grey) and the segregated equilibrium state under illumination with 1 Sun (color) for MAPb(Br$_x$I$_{1-x}$)$_3$ films with different sample composition $\bar{x}$. The PL of the photo-segregated film is independent of $\bar{x}$. b) X-ray diffraction patterns of the 200 (cubic) or 220/004 (tetragonal) reflex for different $\bar{x}$ (X-ray wavelength 1.3401 Å) reveals the compositional dependence of the equilibrium segregated state under illumination. c) Shows that the initial and final position of the center of mass of the patterns remain constant during photo-segregation while a significant shift in the position of the majority phase occurs for Br-rich samples.

with $\bar{x} > 0.5$ exhibit a shift of the most pronounced peak toward higher angles and a long tail toward lower angles. Our results can thus reconcile supposedly conflicting findings of previous reports[1–3,14,22–28] by demonstrating the strong dependence of the structural changes during photo-segregation on the average sample composition.
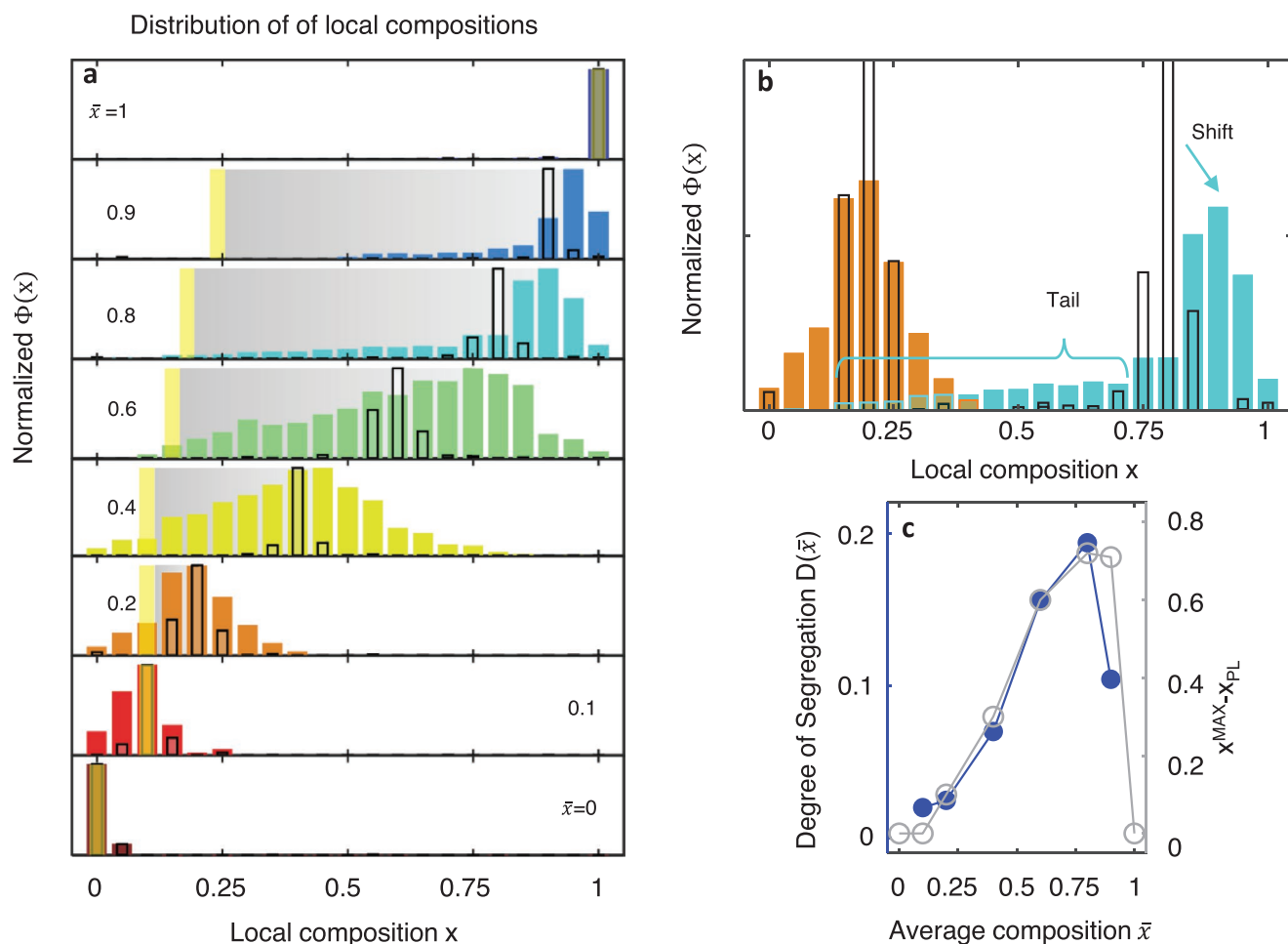
The long tail toward low diffraction angles, evident in the differential XRD pattern (see Note S5, Supporting Information), is only visible for Br-rich compositions. I-rich samples do not exhibit a corresponding tail to higher angles. This asymmetry in the compositional dependence of the XRD patterns of the final equilibrium state under illumination becomes even more evident when translating the XRD-pattern to the compositional phase-distribution discussed in the next section.

From the XRD patterns as well as the PL peak positions, information about the compositional distribution as well as composition of the emissive state can be derived as discussed in Section 5. Here, we assume, that the observed changes in the XRD pattern (broadening, shift and appearing of a tail) are primarily caused by photo-segregation of the samples into domains with differing local compositions. We believe that this is a valid approach as we were not able to reconcile the observed shift, the evolution of a tail and broadening of the experimental XRD patterns in conjunction with their constant COM with changes in strain or crystal domain sizes, (see Notes S3 and S6, Supporting Informtion). We cannot, however, rule out an additional contribution of size effects especially for small I-rich domains.

The normalized compositional phase-distributions in the dark $\Phi_{ini}(x)$ (empty bars) and after an equilibrium distribution has been reached under illumination $\Phi_{fin}(x)$ (color) are shown in **Figure 3**a together with the composition of the emissive phase upon illumination (yellow). $\Phi_{ini}(x)$ is rather narrow and centered around $\bar{x}$ for all samples. Upon illumination a broad distribution of compositional phases forms. Comparing $\Phi_{ini}(x)$ and $\Phi_{fin}(x)$ for all compositions, it becomes obvious, that the equilibrium distribution under illumination depends on the sample composition $\bar{x}$.

In I-rich samples with $\bar{x} < 0.5$, $\Phi_{fin}(x)$ is fairly symmetrically with respect to $\Phi_{ini}(x)$, meaning that we mostly observe a broadening of the phase-distribution. States that are slightly richer in I and Br form almost equally. Contrarily, in Br-rich samples up to 70% of the materials changes its composition. Furthermore, for $\bar{x} > 0.5$ the phase-distribution under illumination appears much more asymmetric compared to the mixed state in the dark. Especially for the samples with $\bar{x} = 0.8$ and $\bar{x} = 0.9$, the majority of the sample adopts a narrow phase-distribution with the maximum centered at higher Br-content. Additionally, a very broad tail toward I-enriched compositions forms. In contrast, I-rich samples, such as $\bar{x} = 0.2$, do not exhibit such a tail neither toward higher Br-content nor toward higher I-content. This becomes even clearer when comparing the $\Phi_{fin}(x)$ for samples of the "mirror" compositions ($\bar{x} = a = 0.2$ and $\bar{x} = 1 - a = 0.8$) in Figure 3b, showing that these phase-distributions are not "mirror images" of each other. This

**ADVANCED
SCIENCE NEWS**

www.advancedsciencenews.com

**ADVANCED
FUNCTIONAL
MATERIALS**

www.afm-journal.de

Figure 3. a) Distributions of local compositions $\Phi(x)$ in the mixed film (empty bars) as well as in the equilibrium state under prolonged illumination (color) are calculated from XRD (See Supporting Information) and compared to the composition of the emissive phase x_{PL} (yellow) calculated from the final PL peak position. In Br-rich samples, the emission stemming from the utmost I-rich domains makes up a minuscule portion of the sample. b) A comparison of the compositional distribution of the mixed and segregated films for $\bar{x} = 0.8$ and $\bar{x} = 0.2$ contrasting the symmetrical broadening of I-rich samples with the asymmetric changes in the compositional distribution for Br-rich samples. c) The degree of segregation $D_{seg}(x)$ increases with increasing bromide content in parallel to the increasing difference in composition between the majority phase x_{MAX} and the emissive phase x_{PL}.

highlights a principal difference between I-rich and Br-rich samples, indicating that iodide and bromide ions are affected differently during the photo-segregation process. The shift of the maximum of the phase-distribution toward higher bromide content and evolution of a long tail distribution of iodide-richer phases can be interpreted as a favored migration of iodide ions out of mixed halide domains causing the parent domain to become iodide depleted and bromide enriched. The migration of iodide into adjacent domains causes a gradient of iodide within the sample leading to the long compositional tail toward higher iodide-content domains.

What we would like to emphasize is that we do not observe the adoption of any preferred compositions comparing samples of different $\bar{x}$ upon illumination. Viewing both XRD and PL data translated to composition as shown in Figure 3a highlights an important fact: While PL measurements allude to the composition of the emissive states, x_{PL}, to be fairly similar for all samples and hence independent of the sample's average composition, XRD measurements reveal that the compositional

distribution $\Phi(x)$ differs strongly between samples. The volume fraction of x_{PL} within $\Phi_{fin}(x)$ becomes smaller with increasing average Br-content. Hence, x_{PL} does hence not reflect the composition of a thermodynamically preferred phase but rather the phase with the highest fraction of iodide within the sample. For Br-rich samples, the relative volume of these domains is so small that it is hardly detectable by XRD. For the $\bar{x} = 0.6$ sample, $x_{PL} \approx 0.1$, which means that the entire PL originates from domains with only 10% bromide that constitute less than 1% of the total sample volume. Thus, the charge-carriers predominantly generated around $x_{MAX} = 0.75$ funnel to only about 1% of the material with $x_{PL} \approx 0.1$.

This charge-carrier funneling leads to an increased charge-carrier concentration within the I-rich domains emission is stemming from. The relative charge-carrier density in the emissive phase $n_{x_{PL}}$ can be estimated in dependence of its volume fraction $\Phi_{x_{PL}}$, as $n_{x_{PL}} \propto 1/\Phi_{x_{PL}}$. Because $\Phi_{x_{PL}}$ is decreasing severely with $\bar{x}$, $n_{x_{PL}}$ follows this dependency. A rough estimate of the relative charge-carrier density is obtained assuming, that nearly

**ADVANCED
SCIENCE NEWS**

www.advancedsciencenews.com

**ADVANCED
FUNCTIONAL
MATERIALS**

www.afm-journal.de

all charge-carriers funnel to the I-rich domains with composition x_{PL}. This is a justified assumption, as the high energy band in PL is quenched entirely during photo-segregation, signifying a depletion of charge-carriers in the Br-rich domains. In a sample with $\bar{x} = 0.2$, $\Phi_{x_{PL}}^{fin} \approx 0.1$ such that the local charge-carrier density in the emissive phase increases by $1/\Phi_{x_{PL}}^{fin} \approx 10$. In a sample with $\bar{x} = 0.8$, where, $\Phi_{x_{PL}} \approx 0.01$ similar domains exhibit a 100 fold increased charge-carrier density. In a segregated sample with $\bar{x} = 0.8$, an illumination with 1 sun, thus results in a local charge-carrier density within the emissive phase, equivalent to illumination with 100 suns. It must be noted that the volume fraction of the emissive phase growths during segregation as discussed in detail in Section 2.2. In the initial stage of phase segregation, the volume fraction is below the detection limit of XRD and thus the charge-carrier densities are likely to be many times larger than estimated for the final segregated state.

In the case of $\bar{x} = 0.1, 0.2$ and 0.4, the XRD data indicates that phases with even higher I-content than x_{PL} form. We cannot rule out, that this is an artefact, due to domain-size related, or phase-transition related broadening/shift of the XRD peaks. If samples indeed exhibit more iodide-rich domains than $x_{PL} \approx 0.1$, we do not observe luminescence from them, which might indicate that they are very defective and hence dark.

As the evolution of the phase-distribution depends significantly on the sample's average composition $\bar{x}$ we introduced a quantitative metric to compare the degree of segregation between samples of different composition, D_{seg}, as defined in Section 5, Equation 7. D_{seg} measures how much the compositional distribution has changed compared to the initial state. This is reflected in $D_{seg}(\bar{x})$ which is proportional to the Br-content (Figure 3c). We do not observe an instability maximum, but rather the instability increases up to $\bar{x} = 0.9$. This trend agrees with the increased difference between the majority phase and the emissive phase $x_{MAX} - x_{PL}$ for higher Br contents.

2.2. Kinetics

The real-time simultaneous in situ measurements of XRD and PL allow us to directly compare and contrast the evolution of the structural changes occurring during phase segregation and the corresponding changes in the emission. The distribution of charge-carriers within the film is responding to changes in the compositional distribution, by localization to emerging low bandgap domains. As the structural changes and the charge-carrier distribution are interdependent, a simultaneous analysis of the evolution of the phase-distribution as well as the low-energy emitting sites can further the understanding of the photo-segregation process.

The evolution of the degree of segregation, $D_{seg}(\bar{x}, t)$, which gives an average measure of how much the sample has changed with respect to the initial dark equilibrium state as a function of time t, allows to directly track how the new phase equilibrium is established under illumination (solid, colored lines **Figure 4**a). The experimental evolution of $D_{seg}(\bar{x}, t)$ follows a simple exponential approximation for all investigated compositions as expected for a first order process. Comparing samples

with different average composition $\bar{x}$, the phase-equilibrium under illumination is established faster for samples with higher bromide content. For a quantitative comparison, we calculated the segregation rate k_{seg} defined as the inverse time needed for $D_{seg}(\bar{x}, t)$ to reach $1/(1 - e) \approx 0.63$ of its maximum value (Figure 4c). We observe that k_{seg} increases with Br-content. For example, the sample with $\bar{x} = 0.9$ segregates almost 6 times faster than the "mirror-composition" sample with $\bar{x} = 0.1$ with rates 0.45 min^{-1} versus 0.08 min^{-1} respectively.

The volume-fraction increase in iodide-rich domains can be quantitatively followed by analyzing the XRD signal in the angular range expected for the composition of low-energy emission sites $I_{XRD}(2\theta)(x = x_{PL}, t)$ (dotted colored lines Figure 4a). In iodide-rich samples, the growth of iodide-rich domains, $I_{XRD}(2\theta)(x = x_{PL}, t)$, correlates with the overall phase-segregation, measured through $D_{seg}(t)$, while in Br-rich samples the growth of domains with a composition of $x = x_{PL}$ is lagging behind the overall phase-segregation. This indicates that in Br-rich samples, the majority of the sample first segregates into bromide and iodide enriched phases close to the mixed composition and in a second step the I-rich tail is formed.

Zooming into the first seconds of photo-segregation, the previously noted complex evolution of PL becomes apparent (Figure 4b).[44] A fast decrease of the high energy emission at 1.93 eV by two orders of magnitude can be seen (stage 1). This decrease in high energy emission is accompanied by the appearance of a low energy PL-peak, which disappears after a few seconds, as we reported previously.[44] The energy of the PL emission can be taken as a measure of which phase is populated with charge-carriers, if band-to-band emission dominant. The fast shift from high-energy PL to low energy PL in stage 1, thus signifies the charge-carrier depletion of Br-rich domains and the charge-carrier funneling to and localization in emerging low energy domains.

As a first approximation, the fraction of the low energy PL ($I_{PL_{low}}/(I_{PL_{low}} + I_{PL_{high}})$) can be used to follow the extend of charge carrier funneling (grey traces in Figure 4a). In comparison to the evolution of $D_{seg}(t)$ and $I_{XRD}(2\theta)(x = x_{PL}, t)$, it becomes evident, that for all samples with $\bar{x} > 0.2$ the charge-carrier localization to I-rich domains occurs rapidly already within the first seconds of phase segregation, prior to any major I/Br ionic reorganization and the growth of a substantial low-bandgap phase in stage 2 (Figure 4a).

The comparison of the kinetics of PL and $D_{seg}(t)$ for different timeframes from seconds to minutes therefore shows that the segregation process is a 2-step process. We conclude that the nucleation and population of nanoscopic I-rich domains, too small to be detectable in XRD is occurring in stage 1, preluding the phase segregation of the bulk material in stage 2.

In numerous studies, the phase-segregation kinetics have been analyzed based on the evolution of the PL signal intensity $I_{PL}(t)$.[1–3,6,7,15,22,23,32,35,44,45] The PL intensity is determined by the absorption of the material and the ratio between radiative and non-radiative recombination kinetics. An increase in emission signal thus signifies a decrease of non-radiative recombination relative to radiative recombination caused by phase-segregation.[7] The PL intensity is, however, not directly connected to
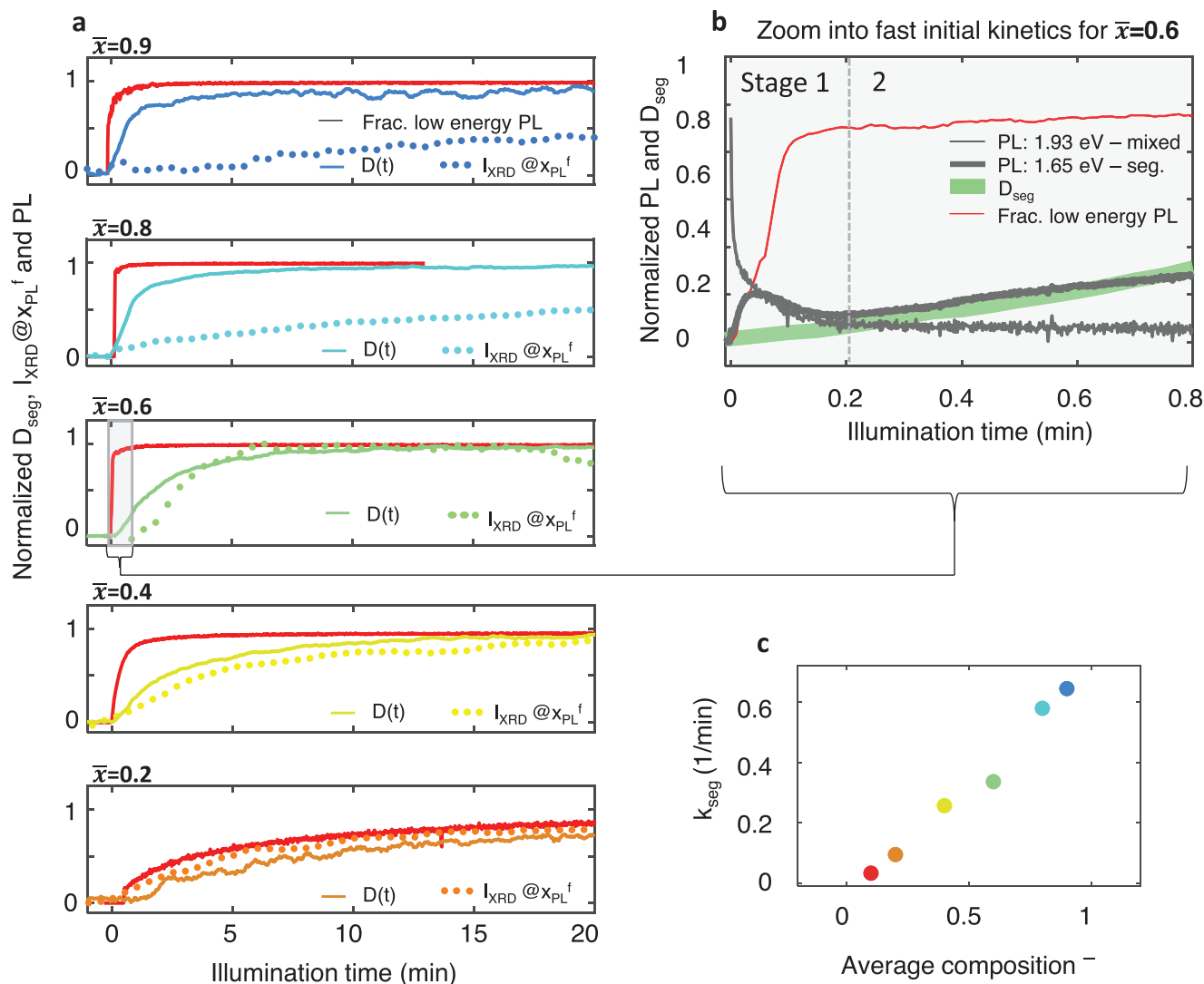
Figure 4. a) The kinetics of the degree of segregation (solid colored line), the XRD intensity of the tail states, corresponding to xPL (colored dotted lines) and the fraction of low energy PL intensity $\frac{I_{PL_{low}}}{I_{PL_{low}} + I_{PL_{high}}}$ (grey) are compared for compositions $\overline{x}$ = 0.2 to 0.9. b) Zoom into the initial phase of photo-segregation. Comparing the evolution of the high energy PL (grey – thin) the low energy PL (grey – bold), the fraction of low energy PL (red) and the segregation kinetics (green) for the sample with $\overline{x}$ = 0.6 shows, that a very fast initial process is occurring in the first seconds corresponding to a rapid charge-carrier depletion of the Br-rich phase, while the macroscopic phase segregation occurs significantly slower at the order of minutes. c) The segregation rates of the slow macroscopic phase segregation increase significantly for Br-rich samples.

the volume fraction of iodide-rich domains. In the Supporting Information, we show that there is indeed a rough correlation between the PL-yield and the degree of phase segregation (Figure S14, Supporting Information). However, this surprising correspondence is only valid for specific, low-bromide sample compositions. Our observation affirms that experimental works utilizing the PL intensity evolution as a probe for the phase-segregation kinetics[1–3,6,7,15,23,28,32,35,44,45] derive roughly valid phase-segregation rates from their experimental data, especially if measurements were carried out on samples with a high-iodide content. PL is, however, not a reliable probe for the phase-segregation kinetics for samples with higher bromide content and should hence not be used as a quantitative probe to study the phase-segregation kinetics.

3. Discussion

The cause of photo-segregation has been postulated to be a charge-carrier-induced transient state. The exact mechanism however, how the excitation of charge-carriers leads to a redistribution of the halide ions within the crystal remains subject of debate. Combining both PL and XRD allows us to directly investigate the interplay of inhomogeneous charge-carrier distribution and structural/compositional rearrangement.

Our experimental results show that, evidently, the photo-induced phase-segregation is an asymmetric process with respect to the halide ratio. There is no mirror symmetry in I-rich and Br-rich samples. This is particularly apparent when comparing the excited state phase-distribution of compositions with

**ADVANCED
SCIENCE NEWS**

www.advancedsciencenews.com

**ADVANCED
FUNCTIONAL
MATERIALS**

www.afm-journal.de

mirror bromide/iodide ratios (e.g., $\overline{x} = 0.2$ and $\overline{x} = 1{-}0.2 = 0.8$), where the phase-distributions of I- and Br-rich samples in the illuminated state do not mirror each other. While in I-rich samples, the phase-distribution merely broadens, in Br-rich samples photo-segregation leads to a change in composition in up to 70% of the material, and a broad distribution of local compositions establishes. Furthermore, the segregation kinetics depend on the sample's average composition exhibiting faster phase-segregation kinetics for samples with higher bromide content. This shows that all aspects of the photo-segregation process, including compositional stability, segregation kinetics, which compositional phases form as well as how much of the material undergoes photo-segregation, depends on the average sample composition. Further, we observe two distinct stages in the segregation kinetics. A temporary low-energy PL peak appears rapidly upon illumination (Figure 4b, stage 1), as discussed in detail in our previous work.[44] At this fast timescale, no change is observable in the XRD patterns yet. The much slower segregation kinetics visible in XRD on the timescale of several minutes and the corresponding slow evolution of the final low energy PL Peak shows that substantial changes in the halide distribution occur only in the second stage, after the formation of I-rich nano-domains and the localization of carriers there (Figure 4b). This highlights the value of using PL and XRD as complementary probes, as PL is very sensitive to the appearance of even miniature I-rich domains. At the same time, XRD provides an accurate picture of the overall compositional phase-distribution in the sample.

3.1. Qualitatively, Charge-Carrier Localization Causes Photo-Segregation Process

Using these experimentally obtained phase-distributions in the segregated state in combination with the segregation kinetics allows us to validate whether previously developed thermodynamic models can describe the observed segregation process. Currently, the predominant theoretical models to describe photo-segregation are the polaron model[15,17,18,37] and a model based on the localization of charge-carriers in low bandgap domains.[7,19,36] Both models assess the compositional photo-stability of Br-I perovskites by estimating whether or not the nucleation of phase-segregation is energetically favorable. Nucleation of phase-segregation here means formation of miniscule I-rich or Br-rich domains as the onset of phase segregation. We assign this nucleation of phase-segregation to the fast initial appearance of low energy PL in stage 1 (see Figure 4b). Often only this initial stage is considered theoretically, without describing the consecutive change of the majority of the material occurring later in time. Further, the models often assume an idealized segregated state consisting of only two phases, a Br-rich phase and an I-rich phase.[7,15,36] As we obviously observe broad and composition-dependent phase-distributions in illuminated samples, we found it necessary expand the theoretical models.

The free energy of mixing is used as a measure for the sample's compositional stability in dependence of the average sample composition. The free energy of mixing $\Delta_{\text{mix}}F(\overline{x})$, is the free energy gain when mixing the pure I and Br phases to form the mixed phase with composition $\overline{x}$, with respective free

energies, F^I, F^{Br}, and F^{mix}. A first approximation of this yields: $\Delta_{\text{mix}}F(\overline{x}) = F^{\text{mix}} - (\overline{x}F^{\text{Br}} + (1-\overline{x})F^I)$. In the excited state, a charge-carrier term has to be added to calculate the free energy of mixing $\Delta_{\text{mix}}F^*$. The nature of this charge-carrier term depends on the model used.[7,15,18,36]

In the polaron model developed by Ginsberg et al., the charge-carriers are assumed to strain the lattice resulting in an additional strain-related energy term, Δg_s, which can be reduced by halide segregation.[15] From the polaron model, the phase compositions of $\overline{x} = 0.2$ and $\overline{x} = 0.8$ are predicted to be energetically favorable and thus most stable under illumination. The predominant formation of these phases, independent of the sample's average composition is expected. The agreement between the theoretical predictions and the experimentally observed PL spectra, was seen as a validation of the polaron model.[15,17,18,37] However, our experimental results show that the compositions of the majority and minority phases strongly depend on the average sample composition $\overline{x}$. For $\overline{x} = 0.6$, we indeed observe a majority phase with $\overline{x} = 0.8$. However, for the sample with $\overline{x} = 0.9$, predicted to be photo-stable in the polaron model, we observe a majority phase, which resembles the pure Br-perovskite instead. We therefore cannot confirm the existence of generally favored compositions. Further, due to the theoretically predicted symmetry of the free energy of mixing and the minimum in free energy for $\overline{x} = 0.8$[15,18] the model fails to describe the asymmetry between I-rich and Br-rich sample's as well as the compositional instability of samples with $\overline{x} \geq 0.8$. We therefore conclude, that the polaron model in its current form cannot be employed to rationalize the full set of our experimental data.

In the charge-carrier localization model, derived by Kuno et al.[7,19] and Bobbert et al.,[36] the formation of a certain amount of I-rich domains is favorable, as it allows the sample under illumination to reduce its free energy by localization of charge-carriers in the I-rich domains, were the bandgap E_G is substantially smaller. In the mixed state the energy of the charge-carriers $N \cdot E_G(\overline{x})$, where N is the number of charge-carriers and $E_G(\overline{x})$ is the bandgap of the mixed material. As shown schematically for a sample with $\overline{x} = 0.8$ (**Figure 5**d,e), if the sample is in the dark, only the mixed phase exists with $x = 0.8$ with a free energy $F(\overline{x})$. Under illumination the free energy is increased by the energy of the charge-carriers $F^*(\overline{x}) = F(\overline{x}) + N \cdot E_G(\overline{x})$. The free energy of the illuminated state is thus a function of the number of excited states N as well as the bandgap of the material E_G. The increase in energy is thus higher for bromide-rich samples, which have a higher bandgap. However, it can be effectively reduced by charge-carrier funneling into pre-existing or randomly created small I-rich domains to $N \cdot E_G(x_{\text{PL}})$, where x_{PL} is the composition of the emissive phase.[7,19,36] The difference in bandgap between the mixed phase and the I-rich phase therefore provides a thermodynamic driving force for the formation of I-rich domains. This model predicts the free energy of mixing under illumination to be bandgap dependent and thus asymmetric and almost linearly increasing with increasing Br-content. This agrees with the herein observed higher final degree of segregation, D_{seg} with higher bromide-content, shown in Figure 3.

Considering the formation of an I-rich phase and charge-carrier funneling to these domains is enough to rationalize the experimentally observed compositional distribution established under illumination. In Br-rich samples, the majority phase is
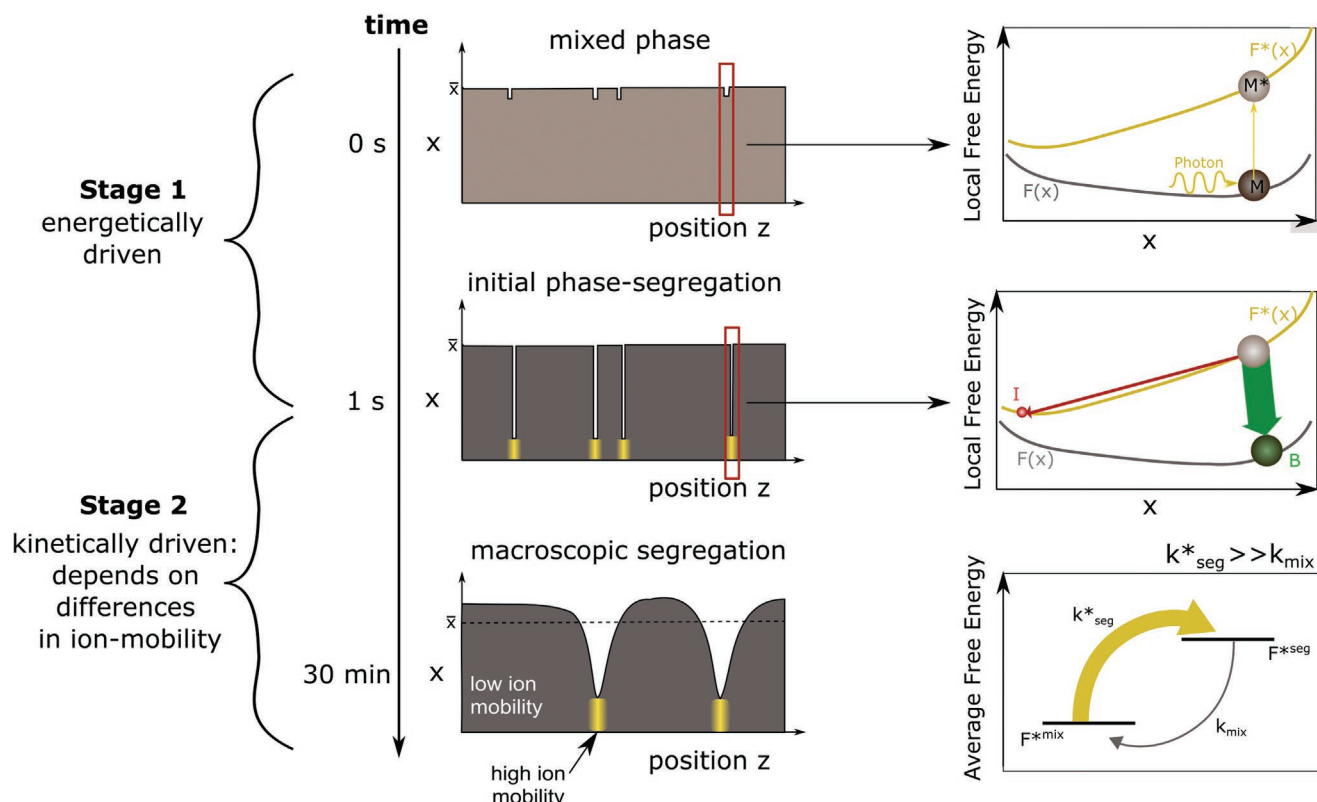
Figure 5. In stage 1, nanoscale segregated domains are formed. Their formation is locally energetically favorable as indicated in the energy schematics (right side). The presence of I-rich domains (red ball) in close vicinity to charge-carrier generation allows for the reduction of charge-carrier energy via funneling to such low bandgap, I-rich domains. The bromide rich phase (green ball) is thus depleted of charge-carriers and is effectively in the dark. Triggered by the nucleation of I-rich domains, the sample undergoes macroscopic photo-segregation in stage 2, which is kinetically stabilized by a difference between fast segregation rates and slow recovery rates, as indicated in, as indicated in the energy diagram corresponding to the entire sample.

nearly completely deprived of charge-carriers. This phase is thus stabilized because it is virtually in the dark as all charge-carriers funnel to few low-bandgap domains. Which composition the majority phase adopts thus depends merely on the sample's average composition and on how much iodide is accumulated in the iodide rich phase, following $x_{Br} \approx \overline{x} - \Phi_{x_{PL}} \cdot x_{PL}$ with $\Phi_{x_{PL}}$ being the volume fraction of the iodide rich phase. This agrees with the experimentally observed composition-dependence of the majority distribution. A second energetic minimum to rationalize the formation of a bromide-rich phase is thus not needed: Because the majority distribution is virtually in the dark, it is striving to stay mixed. The width of the majority distribution is thus observed to be narrower in Br-rich samples than in I-rich samples. In I-rich samples, the charge-carrier distribution is expected to be more homogeneous. We thus conclude that the charge-carrier localization model is qualitatively describing the experimental observed asymmetry of the photo-segregation process and the observed compositional distribution very well.

3.2. Quantitatively, the Charge-Carrier Density is Too Low to Segregate the Entire Sample

We further set out to assess whether the thermodynamic charge-carrier localization model can describe the experimentally

observed extent of segregation quantitatively. In a static picture, one state is favored over the other if it is lower in energy. In the charge-carrier localization model, this means that under illumination, the energy of the segregated state, with all the charge carriers in the low bandgap phase, needs to be less than that of the mixed state, with all charge carriers in the higher bandgap phase.

We use the experimentally obtained volume fractions $\varphi(x_m)$ to approximate $\Phi(x)$ and the PL energy to estimate the energy of the charge carriers. We can thus calculate this difference in free energy $\Delta E^*(\overline{x}) = F^*_{mix}(\overline{x}) - F^*_{seg}(\overline{x})$ directly, while relying on literature values for the free energy in the dark.

Distinct equations can be derived for the illuminated state free energy in the segregated state and the mixed state.

$$F^*_{mix}(\overline{x}) = \underbrace{F(\overline{x})}_{dark} + \underbrace{N \cdot E_G(\overline{x})}_{charge\ carrier\ term} \tag{1}$$

$$F^*_{seg}(x) = \underbrace{\int_0^1 \Phi^{seg}(x) \cdot F(x)\,dx}_{dark} + \underbrace{N \cdot E_G(x_{PL})}_{charge\ carrier\ term} \tag{2}$$

The number of charge carriers N is proportional to the generation of charge carriers and their lifetimes. In a first approximation, we assume N not to change during phase-segregation.

**ADVANCED
SCIENCE NEWS**

www.advancedsciencenews.com

**ADVANCED
FUNCTIONAL
MATERIALS**

www.afm-journal.de

The energy gained by segregation can therefore be expressed as:

$$\Delta E^*(\overline{x}) = F_{mix}^*(\overline{x}) - F_{seg}^*(x)$$

$$= \underbrace{\underbrace{F(\overline{x})}_{dark} + \underbrace{N \cdot E_G(\overline{x})}_{charge\ carrier}}_{mixed} - \underbrace{\underbrace{\int_0^1 \Phi^{seg}(x) \cdot F(x)\, dx}_{dark} + \underbrace{N \cdot E_G(x_{PL})}_{charge\ carrier}}_{segregated}$$

$$= \underbrace{F(\overline{x}) - \int_0^1 \Phi^{seg}(x) \cdot F(x)\, dx}_{dark} + \underbrace{N \cdot \left(E_G(\overline{x}) - E_G(x_{PL})\right)}_{charge\ carrier} \quad (3)$$

In the dark, if $N = 0$, $\Delta E^*(x)_{N=0}$ is negative for all compositions, showing that, without the contribution of charge-carriers, the segregated state is energetically unfavorable. As expected, our estimation thus yields, that phase-segregated samples will recover in the dark, in line with the reversibility of the phase-segregation observed experimentally.[1]

The phase segregation may become energetically favorable if the charge-carrier contribution is large enough.

$$N\left(E_G(x_{PL}) - E_G(\overline{x})\right) > F(\overline{x}) - \int_0^1 \Phi^{seg}(x) \cdot F(x)\, dx \quad (4)$$

As the charge-carrier term scales with N, a more detailed look at realistic charge-carrier densities is needed to assess whether segregation is predicted to be favorable under realistic conditions.

The thermodynamic models, predicting photo-segregation to be energetically favorable, do their predictions based on a simplified model system. Either very high charge-carrier densities have been assumed with n on the order of one charge-carrier per formula unit (f.u.)[7,18] (formula unit is MAPb(I,Br)$_3$ which has a volume of ≈0.25 nm[3]).[36] Or only the very initial stage of photo-segregation with $\Phi(x_{PL}) \approx 0$ and thus hardly any change in the compositional distribution is considered.[36] Gao et al. consider a polaronic strain of $\delta = 0.15$, which is only plausible to occur very localized around each excitation. At reasonable excitation densities this does not reflect the average strain of the entire sample.[18]

With an excitation density of 100 mW cm^{-2} (≈1 sun) at 453 nm, and a charge-carrier lifetime of 100 ns, which is reasonable metal halide perovskites,[46] the average charge-carrier density is ≈$n = 1.5 \times 10^{-6}$ nm^{-3} (which is 1.5×10^{15} cm^{-3} n or 4×10^{-7}/f.u.). In a grain, 300 nm × 300 nm × 200 nm, this corresponds to 25 charge-carriers only. The reduction in energy of these 25 charge-carriers needs to be enough to segregate the entire grain. The blue line in **Figure 6**, shows that under the experimental conditions, the contribution of the mean charge-carrier density is not sufficient to explain the extend of photo segregation, experimentally observed, where up to 70% of the material undergo a change of their composition. The segregated state only becomes stable under the assumption of unreasonable large charge-carrier lifetimes on the order of 1 ms (Note S11, Supporting Information). We therefore conclude, that the experimentally observed equilibrated segregated state, is not energetically favorable over the mixed state at an excitation density corresponding to 1 Sun.
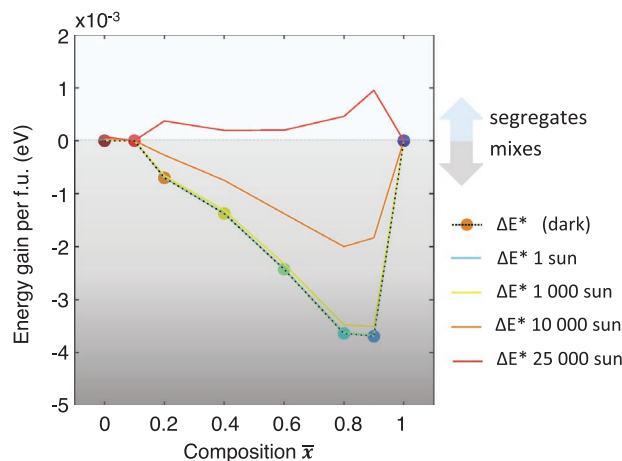
Figure 6. Shows that in the dark the energy gained by segregation is negative for all compositions indicating that the segregated state is unstable and will remix in the absence of charge-carriers. For an excitation with $\lambda = 453$ nm equivalent to 1 sun (100 mW cm^{-2}), $\tau = 100$ ns, and homogeneously distributed charge-carriers (turquoise) the charge carriers do not possess enough energy to segregate the sample. The energy gained by segregation for higher excitation densities, which may locally be reached by different degrees of charge-carrier accumulations in iodide rich domains are shown in colored lines. At least 25 000× increase in charge-carrier density is needed to stabilize the segregated state.

3.3. Charge-Carrier Funneling Enables Phase Segregation Locally

However, as discussed in Section 2.1, the charge-carrier funneling to very small domains creates locally very high charge-carrier densities. Such high charge carrier densities can rationalize the initial stage of phase-segregation, as predicted by theoretical modeling.[7,36,37] In Figure 6 the colored lines indicate the energy gained by segregation for the excited state for different charge-carrier concentrations n_I within the I-rich domains. The segregated state only becomes locally energetically favourable assuming high local charge-carrier concentrations $n_I = 25000 \times n$. This is the case, if all charge-carriers generated in the exemplarily 300 nm × 300 nm × 200 nm grain funnel to a 5 nm × 5 nm × 5 nm cube.

Both, models based on the localization of charge-carriers as well as the polaron model, are static models, were charge-carriers only have a momentary effect, which is gone once the charge-carriers recombine. Each charge-carrier can only have a small effect due to their limited energy of ≈2 eV. At moderate charge-carrier densities, found for 1 sun, only a very small volume fraction of the material around 10^{-6} can therefore be rationalized to segregate. This is corresponding to the initial state of phase segregation and in line with the theoretically predicted phase-segregated nuclei of ≈1 nm in size.[7] We propose that the initial rapid appearance of a low energy PL peak, prior to the macroscopic photo-segregation indeed corresponds to the appearance of such locally segregated domains, which are too small to be visible in XRD. As observed from the PL kinetics (Figure 4b), already after a few seconds the entire emission is stemming from I-rich domains. In this initial stage of phase segregation, miniscule I-rich domains allow for effective reduction of the charge-carrier energy but no substantial changes

**ADVANCED
SCIENCE NEWS**

www.advancedsciencenews.com

**ADVANCED
FUNCTIONAL
MATERIALS**

www.afm-journal.de

in the compositional distribution have yet occurred, such that the "dark energy term" is virtually staying constant. While it becomes clear, that such a state will be thermodynamically preferred, it is not trivial to rationalize why the sample continuous to segregate over a time of 30 min leading to the majority of the sample to change its composition. We concluded that to explain the evolution of phase-segregation, other factors, and phenomena needed to be considered.

3.4. Charge-Carrier Localization Causes Accumulative Changes in the Material

To rationalize the extended phase-segregation toward the final phase-segregated state under illumination, we propose a dynamic picture in which the accumulative energy exerted on the sample by continuous irradiation leads to long-lived changes to the material. Kuno et al. developed a phenomenological kinetic model in which it is pointed out, that in addition to an energetic driving force, the differences between the phase-segregation rate and recovery (remixing) rate determine the final state under illumination of a sample.[7] We here go beyond this and propose that a light-induced spatial inhomogeneity of segregation and recovery rates, is needed to explain the latter stage of macroscopic photo-segregation.

We propose that this inhomogeneity is caused by a prevalent form of photo-induced halide vacancies in I-rich domains resulting in spatially inhomogeneous ion mobilities. The role of halide-vacancies as an accelerating factor for photo- segregation has recently been reviewed by Tian et al.[47] the main mechanism is that ion-migration, which is the key pre-requisite for both segregation and recovery, predominantly occurs via vacancy-mediated diffusion of halide ions.[6,12,39,48–50] During the initial stage of phase segregation, it has been shown by Tiede et al. and Suchan et al. that the pre-existing vacancy density determines the location of segregated domains and their segregation kinetics.[44,50] This again highlights the importance of the defect density in the phase segregation process, especially when looking at the initial stage of segregation. However, next to pre-existing halide vacancy densities, photo-induced vacancies via the weakening of Pb—I bonds need to be considered to understand the continuous process.[39–41,49] They are likely the major reason behind the reported excitation-density dependence of the ion mobility [39,40,49,51–54] and have recently been suggested to be an underlying factor determining phase segregation.[38]

In the case of mixed halide perovskites, the inhomogeneous charge carrier density implies that photoinduced effects primarily occur in the I-rich domains. The concentration of charge-carriers in "hot-spots", leads to a higher probability of oxidation and creation of halide vacancies there, than expected for irradiation with 1 sun. By continuous irradiation, local high iodide vacancy densities are thus built up, which results in locally enhanced ionic mobility. This inhomogeneous ion-mobility leads to large differences between k_{seg} and k_{mix}. The phase segregation which is only occurring in the "hot spots" with high ionic mobility will be very fast. On the contrary, the recovery which occurs in the charge-carrier-deprived majority of the sample, where the ionic mobility is expected to be much smaller, will be slow. This leads to an overall much higher segregation rate than the recovery rate, as indicated in Figure 5. Once segregated regions will thus remain segregated long after the charge-carriers have recombined.

This proposition is corroborated by the experimentally observed acceleration of segregation for Br-rich samples (x = 0.9), by a factor of 6 compared to x = 0.2. This lack of such large differences in the recovery rates in the dark, discussed in Supporting Information Note S10, clearly shows that the observed acceleration of segregation in Br-rich samples is a light-induced effect, rather than due to generally higher ion mobility in Br-rich samples. The stronger local charge-carrier concentration in Br-rich samples leads to higher local vacancy and interstitial densities. From the phase-distribution of the final segregated state, we estimate as a lower limit a 10-fold higher local charge carrier concentration in Br-rich samples compared to I-rich samples. However, we anticipate, that this difference is even larger in the initial stage of phase-segregation, when the I-rich domains are below the detection limit of XRD. Higher spatial inhomogeneity in the vacancy density in Br-rich samples can thus well rationalize the faster segregation in the Br-rich samples.

How this mechanism leads to gradual phase-segregation needs to be investigated further. We here like to formulate some hypothesis, which we hope can guide the development of more advanced models and experiments to be verified or disproven. In an initial step, charge carriers accumulate on statistically-appearing low-bandgap domains. In these "hot-spots" the local charge-carrier density becomes very high and the phase-segregated state becomes energetically favored, in line with the charge carrier localization models. Almost pure I-rich domains in close proximity to Br-enriched domains are formed, corresponding to Stage 1 in Figure 5. Inter-diffusion between I-rich and Br-rich domains leads to local re-equilibration and concentration gradients, especially when domains are de-excited and the driving force for phase-segregation disappears. Due to the relatively larger energetic depth of iodide-rich domains in very high bromide-content surrounding, charge carriers funneling into newly appearing low-bandgap domains caused by random fluctuations – "hot spots" – is preferred and a new area being segregated. Continuation of this may lead to a spot-by-spot segregation. Further kinetic modeling should therefore include the interplay between inhomogeneous and dynamically changing segregation rates as well as continuous slow diffusion-driven remixing and continuous appearance of new I-rich domains due to random fluctuations.

Our results highlight the importance of photo-induced dynamically changing material properties in metal halide perovskites. To assume constant defect concentrations during illumination falls short of reality in most cases. Dynamic defect concentrations have been reported as plentiful and are present in all metal halide perovskites independent of the halide mixture.[55–60] The resultant dynamic ion mobility is the underlying cause of light- and charge-carrier-induced effects such as hysteresis, photo-enhancement, and photo-bleaching, as well as the remarkable recovery and self-healing capabilities of metal halide perovskites. Mixed halide perovskites present a special model system in which dynamic changes in ion mobility determine the phase segregation-process and become uniquely apparent and examinable.

**ADVANCED
SCIENCE NEWS**
www.advancedsciencenews.com

**ADVANCED
FUNCTIONAL
MATERIALS**
www.afm-journal.de

4. Conclusion and Outlook

While a multitude of diverse approaches have been developed to rationalize the photo-induced phase-segregation there is a discontinuity between thermodynamic models rationalizing the initial stage of phase-segregation and models phenomenologically describing the latter stage of phase-segregation and its kinetics. To reconcile both regimes, we propose that a dynamic model is needed, considering the accumulation of light-induced material perturbations during continuous irradiation.

Qualitative comparison of our experimental results with current thermodynamic models reveals that the phase-distribution established during phase-segregation as well as the stability of the samples is likely to be determined by the energy gain of charge-carriers localizing in randomly appearing I-rich domains and therefore initializing nanoscopic phase-segregation. Both, the charge-carrier localization model and the polaron model rely on the energy of the average charge-carrier distribution and static material properties. However, a quantitative comparison of the final equilibrium state reached during illumination, yields that the energy of the average charge-carrier density is not sufficient to rationalize the severity of the segregation.

Our experimental data gives quantitative insight into the full range of phases forming during segregation, their kinetics as well as the simultaneous evolution of the emissive phase for a complete set of sample compositions. We are confident that this unique set of structural, kinetic, and optical data delivers a basis for developing more sophisticated models, which consider the dynamic nature of metal halide perovskites.

As the exact mechanism behind the suggested gradual segregation will have to be explored. Based on the experimental findings described herein, we would here like to propose several hypotheses, to guide further experimental and theoretical works:

1) The localization of charge-carriers on low-energy sites leads to an inhomogeneous charge-carrier density and may lead to the preferential generation of iodide vacancies and interstitials
2) Due to differences in local ionic defect concentrations, there are differences in the segregation and remixing rates in charge carrier enriched (excited) and charge carrier deprived (dark) domains
3) Macroscopic phase-segregation occurs spot-by-spot through accumulative changes in the material
4) In addition to drift, diffusion-driven ionic transport due to gradients in the iodide vacancy and interstitial concentrations need to be considered

5. Experimental Section

Experimental Design: To follow the emergence of iodide-rich domains and their population with charge-carriers, as well as changes in the microscopic sample composition during illumination, we measured X-ray diffraction (XRD), and photoluminescence (PL) signals simultaneously at the same area of interest. For this, we designed a custom-built experimental chamber, shown in Figure 1a. For sample illumination and PL excitation, a blue LED centered at 453 nm was used and calibrated to 0.1 W cm^{-2} power density at the sample surface (1 Sun). The integration

time for the PL spectra was set to 100 ms or 500 ms depending on the samples' luminescence yield for the initial 50 s. Beyond this, the integration time was set to 5 s. The experimental setup was designed to maintain a controlled atmosphere and constant temperature during the experiment. In the experiments reported here, the sample was kept in a nitrogen atmosphere at 20 °C, since the photo-segregation process has been shown to be atmosphere[32] and temperature-dependent[18,61] (see Supporting Information Note S13) For the in situ XRD measurements, the high-flux GaKα radiation of a liquid metal-jet X-ray source in combination with an area detector was used.[62,63] Due to the splitting of the GaKα line into GaKα_1 and GaKα_2, the measured XRD patterns of the homogeneous samples show a double peak for each reflection. (see Note S1, Figure S2, Supporting Information).

The integration time for all segregation measurements was fixed to 3 s per image, with a dead-time of 0.12 s between each image. For the remixing experiments the integration time was also set to 3 s per image initially but was increased to 1 min after the initial hours to reduce the data size.

The initial and final patterns represent equilibrium states (in the dark and under illumination respectively) at which no changes in time are observed in the patterns. 50 patterns were integrated to achieve a better signal to noise ratio in patterns displayed in Figure 2b.

Samples: Here, methylammonium lead bromide/iodide, MAPb(Br$_x$I$_{1-x}$)$_3$ samples were studied. The average composition, $\bar{x}$, of the samples was defined as $\bar{x}$ = [Br]/([I]+[Br]). Samples with the average sample compositions of $\bar{x}$ = 0, 0.1, 0.2, 0.4, 0.6, 0.8, 0.9, and 1 were studied. As the sample's phase-distribution and hence ionic homogeneity varies during the photo-segregation process, it was important to distinguish the local halide composition of a sub-phase, x, within the phase-distribution, $\Phi(x)$ from the average halide composition of the sample, $\bar{x}$, assumed to be equivalent to the halide ratio in the precursor solutions used for depositing the samples. Samples were prepared according to procedures described previously and details can be found in the Note S1 (Supporting Information).[44,64]

Analysis Procedures: Exemplary PL and XRD measurement data acquired during illumination are shown in Figure 1c,b for the sample with $\bar{x}$ = 0.6. It shows the shift of the PL peak energy from 1.9 eV to 1.7 eV upon illumination as previously reported (Figure 1b).[1,2,15,27,65] Simultaneously recorded changes in the 200 XRD reflex of the cubic $Pm\bar{3}m$[66] phase can be seen: the diffraction peak, initially centered at 25.5°, broadened remarkably upon illumination of the sample. Here, the analysis was carried out on the 200 peaks but the behavior was also observed for other reflexes in the detection range as discussed in the SI (see Note S1, Figure S3, Supporting Information for all full patterns from 10° to 32°). It must be noted that both the XRD pattern and the PL spectra reach an equilibrium where further changes are negligible. This state was considered to be the equilibrium phase-distribution under illumination. In the case of $\bar{x}$ = 0.6, this equilibrium was reached after 20 min, as indicated by a dashed line in Figure 1b,c.

During illumination of the samples, it was checked that the light-induced phase-segregation was predominantly observed and not photo-degradation effects or the formation of other secondary phases by evaluating the center of mass (COM) of the XRD diffraction patterns, defined as:

$$COM = \int I_{XRD}(2\theta)\, 2\theta\, d\theta\, /\, \int I_{XRD}(2\theta)\, d\theta \tag{5}$$

where $I_{XRD}(2\theta)$ is the XRD intensity at 2θ. Neither the COM nor the integrated area under a specific XRD-peak, $\int I_{XRD}(2\theta)$, changed during the duration of the illumination, as discussed in Notes S2 and S3 (Supporting Information). This confirms that no non-perovskite secondary phases are formed, no material is lost (e.g., by evaporation or other degradation processes), and neither are amorphous phases formed at the time-scale of the experiment.

An analysis procedure was developed to translate both the PL peak position as well as the XRD diffraction pattern to the composition or compositional distribution, $\Phi(x)$, within the MAPb(Br$_x$I$_{1-x}$)$_3$ samples.

This enabled to directly compare, and contrast compositional information gathered from the PL and XRD signatures from the samples under investigation. To translate the experimentally detected PL peak energy to a specific composition, x_{PL}, a calibration curve relating the PL peak position to the halide composition was used, as discussed in Figure S8 (Supporting Information).[1,20,42,67] The phase-distribution, $\Phi(x)$, is derived from the XRD patterns, $I_{XRD}(2\theta)$. For this, the continuous phase-distribution $\Phi(x)$ was approximated by a discrete function φ_m with 21 different compositions x_m indexed by $m = 1, 2, ..., 21$. A corresponding XRD pattern can then be calculated for the distribution φ_m through a linear combination of reference diffraction patterns $I_{XRDm}(2\theta)$ expected for samples with different compositions Reference patterns, $I_{XRDm}(2\theta)$, were patterned with x_m ranging from 0 to 1 in steps of 0.05 assuming that the XRD peak shapes are equal to the instrumental response function (IRF) at the diffraction angles expected for the specific composition $2\theta(x_m)$. These reference patterns were used to calculate the linear combination coefficients φ_m:

$$I_{XRD}(2\theta) = \sum_{m=1}^{21} \varphi_m I_{XRD_m}(2\theta) \tag{6}$$

where the coefficient φ_m is the volume fraction of the sample in the phase with composition x_m. This procedure assumed that the width of the diffraction peaks in the dark and under illumination is dominated by compositional inhomogeneity and neither strain nor size. This assumption is justified in Notes S3 and S6, where from both Williamson–Hall analysis and the analysis of the peak shape, it is shown that peak-broadening is not consistent with changes in the domain size nor strain in the samples under investigation.

To quantify and compare the extent of phase-segregation between samples, the degree of segregation, $D_{seg}(\bar{x})$, was introduced. The degree of segregation measures how much the compositional distribution is different from that expected for an ideal homogeneous sample of composition $\bar{x}$ normalized to the state where the sample is segregated entirely into pure iodide and pure bromide domains (as illustrated in Figure S13, Supporting Information). Thus, it is defined as the ratio between the variance of the distribution $Var(\Phi(x,\bar{x}))$ and the maximum possible variance, $Var(\Phi_{max,seg}(x,\bar{x}))$ for a given composition $\bar{x}$:

$$D_{seg}(\bar{x}) = \frac{Var(\Phi(x\bar{x}))}{Var(\Phi_{max\,seg}(x,\bar{x}))} \approx \frac{\sum_{n=1}^{21} \varphi(x_m)[x_m - \bar{x}]^2}{(1-\bar{x})\bar{x}^2 + \bar{x}(1-\bar{x})^2} = \frac{\sum_{n=1}^{21} \varphi(x_m)[x_m - \bar{x}]^2}{2\bar{x}(1-\bar{x})} \tag{7}$$

The maximum variance for a composition $\bar{x}$, $Var(\Phi_{max\,seg}(x,\bar{x}))$ is reached when the sample is completely segregated into the pure halide compounds MAPbI$_3$ and MAPbBr$_3$: $\Phi_{max\,seg}(0) = 1 - \bar{x}$, $\Phi_{max\,seg}(0 < x < 1) = 0$ and $\Phi_{max\,seg}(1) = \bar{x}$. The maximum relative amount of MAPbI$_3$ and MAPbBr$_3$ are defined by the average sample composition $\bar{x}$. As an example for the sample with x = 0.6, $Var(\Phi_{max\,seg}(x, 0.6))$ would be reached when the sample is fully segregated into MAPbI$_3$ and MAPbBr$_3$ with a 40% and 60% volume fraction, respectively. The degree of segregation, $D_{seg}(\bar{x})$, is thus a quantitative metric expressing the phase-distribution function $\Phi(x)$ as a single number. We found $D_{seg}(\bar{x})$ a useful metric to compare samples of different compositions and their temporal evolution of the phase-segregation, $D_{seg}(\bar{x},t)$ quantitatively.

Supporting Information

Supporting Information is available from the Wiley Online Library or from the author.

Acknowledgements

Conflict of Interest

The authors declare no conflict of interest.

Data Availability Statement

The data that support the findings of this study are available from the corresponding author upon reasonable request.

Keywords

[1] E. T. Hoke, D. J. Slotcavage, E. R. Dohner, A. R. Bowring, H. I. Karunadasa, M. D. McGehee, *Chem. Sci.* **2014**, *6*, 613.

[2] D. J. Slotcavage, H. I. Karunadasa, M. D. McGehee, *ACS Energy Lett.* **2016**, *1*, 1199.

[3] M. C. Brennan, S. Draguta, P. V. Kamat, M. Kuno, *ACS Energy Lett.* **2018**, *3*, 204.

[4] M. C. Brennan, A. Ruth, P. V. Kamat, M. Kuno, *Trends Chem.* **2020**, *2*, 282.

[5] E. L. Unger, L. Kegelmann, K. Suchan, D. Sörell, L. Korte, S. Albrecht, *J. Mater. Chem. A* **2017**, *5*, 11401.

[6] A. Ruth, M. C. Brennan, S. Draguta, Y. V. Morozov, M. Zhukovskyi, B. Janko, P. Zapol, M. Kuno, *ACS Energy Lett.* **2018**, *3*, 2321.

[7] S. Draguta, O. Sharia, S. J. Yoon, M. C. Brennan, Y. V. Morozov, J. S. Manser, P. V. Kamat, W. F. Schneider, M. Kuno, *Nat. Commun.* **2017**, *8*, 200.

[8] W. Rehman, R. L. Milot, G. E. Eperon, C. Wehrenfennig, J. L. Boland, H. J. Snaith, M. B. Johnston, L. M. Herz, *Adv. Mater.* **2015**, *27*, 7938.

[9] W. Rehman, D. P. McMeekin, J. B. Patel, R. L. Milot, M. B. Johnston, H. J. Snaith, L. M. Herz, *Energy Environ. Sci.* **2017**, *10*, 361.

[10] S. Draguta, J. A. Christians, Y. V. Morozov, A. Mucunzi, J. S. Manser, P. V. Kamat, J. M. Luther, M. Kuno, *Energy Environ. Sci.* **2018**, *11*, 960.

[11] G. F. Samu, C. Janáky, P. V. Kamat, *ACS Energy Lett.* **2017**, *2*, 1860.

[12] K. Datta, B. T. van Gorkom, Z. Chen, M. J. Dyson, T. P. A. van der Pol, S. C. J. Meskers, S. Tao, P. A. Bobbert, M. M. Wienk, R. A. J. Janssen, *ACS Appl. Energy Mater.* **2021**, *4*, 6650.

[13] A. Singareddy, U. K. R. Sadula, P. R. Nair, *J. Appl. Phys.* **2021**, *130*, 225501.

[14] C. M. Sutter-Fella, Q. P. Ngo, N. Cefarin, K. L. Gardner, N. Tamura, C. V. Stan, W. S. Drisdell, A. Javey, F. M. Toma, I. D. Sharp, *Nano Lett.* **2018**, *18*, 3473.

[15] C. G. Bischak, C. L. Hetherington, H. Wu, S. Aloni, D. F. Ogletree, D. T. Limmer, N. S. Ginsberg, *Nano Lett.* **2017**, *17*, 1028.

[16] F. Brivio, C. Caetano, A. Walsh, *J. Phys. Chem. Lett.* **2016**, *7*, 1083.

[17] C. G. Bischak, A. B. Wong, E. Lin, D. T. Limmer, P. Yang, N. S. Ginsberg, *J. Phys. Chem. Lett.* **2018**, *9*, 3998.

[18] X. Wang, Y. Ling, X. Lian, Y. Xin, K. B. Dhungana, F. Perez-Orive, J. Knox, Z. Chen, Y. Zhou, D. Beery, K. Hanson, J. Shi, S. Lin, H. Gao, *Nat. Commun.* **2019**, *10*, 695.

[19] I. M. Pavlovetc, A. Ruth, I. Gushchina, L. Ngo, S. Zhang, Z. Zhang, M. Kuno, *ACS Energy Lett.* **2021**, *6*, 2064.

[20] E. M. Hutter, L. A. Muscarella, F. Wittmann, J. Versluis, L. McGovern, H. J. Bakker, Y.-W. Woo, Y.-K. Jung, A. Walsh, B. Ehrler, *Cell Rep Phys Sci* **2020**, *1*, 100120.

[21] C. M. Sutter-Fella, Y. Li, M. Amani, J. W. Ager, F. M. Toma, E. Yablonovitch, I. D. Sharp, A. Javey, *Nano Lett.* **2016**, *16*, 800.

[22] S. J. Yoon, S. Draguta, J. S. Manser, O. Sharia, W. F. Schneider, M. Kuno, P. V. Kamat, *ACS Energy Lett.* **2016**, *1*, 290.

[23] A. J. Barker, A. Sadhanala, F. Deschler, M. Gandini, S. P. Senanayak, P. M. Pearce, E. Mosconi, A. J. Pearson, Y. Wu, A. R. Srimath Kandada, T. Leijtens, F. De Angelis, S. E. Dutton, A. Petrozza, R. H. Friend, *ACS Energy Lett.* **2017**, *2*, 1416.

[24] M. Hu, C. Bi, Y. Yuan, Y. Bai, J. Huang, *Adv. Sci.* **2016**, *3*, 1500301.

[25] X. Yang, X. Yan, W. Wang, X. Zhu, H. Li, W. Ma, C. Sheng, *Org. Electron.* **2016**, *34*, 79.

[26] F. Lehmann, A., M. Franz, D. Többens, S. Levcenco, T. Unold, A. Taubert, S. Schorr, *RSC Adv.* **2019**, *9*, 11151.

[27] T. Duong, H. K. Mulmudi, Y. Wu, X. Fu, H. Shen, J. Peng, N. Wu, H. T. Nguyen, D. Macdonald, M. Lockrey, T. P. White, K. Weber, K. Catchpole, *ACS Appl. Mater. Interfaces* **2017**, *9*, 26859.

[28] A. J. Knight, J. Borchert, R. D. J. Oliver, J. B. Patel, P. G. Radaelli, H. J. Snaith, M. B. Johnston, L. M. Herz, *ACS Energy Lett.* **2021**, *6*, 799.

[29] H. Zhang, X. Fu, Y. Tang, H. Wang, C. Zhang, W. W. Yu, X. Wang, Y. Zhang, M. Xiao, *Nat. Commun.* **2019**, *10*, 1088.

[30] H. Funk, O. Shargaieva, A. Eljarrat, E. L. Unger, C. T. Koch, D. I.n Abou-Ras, *J. Phys. Chem. Lett.* **2020**, *11*, 4945.

[31] J.-W. Lee, S.-H. Bae, N. De Marco, Y.-T. Hsieh, Z. Dai, Y. Yang, *Mater. Today Energy* **2018**, *7*, 149.

[32] A. J. Knight, A. D. Wright, J. B. Patel, D. P. McMeekin, H. J. Snaith, M. B. Johnston, L. M. Herz, *ACS Energy Lett.* **2018**, *4*, 75.

[33] R. A. Belisle, K. A. Bush, L. Bertoluzzi, A. Gold-Parker, M. F. Toney, M. D. McGehee, *ACS Energy Lett.* **2018**, *3*, 2694.

[34] W. Mao, C. R. Hall, S. Bernardi, Y.-B. Cheng, A. Widmer-Cooper, T. A. Smith, U. Bach, *Nat. Mater.* **2021**, *20*, 55.

[35] T. Elmelund, B. Seger, M. Kuno, P. V. Kamat, *ACS Energy Lett.* **2020**, *5*, 56.

[36] Z. Chen, G. Brocks, S. Tao, P. A. Bobbert, *Nat. Commun.* **2021**, *12*, 2687.

[37] D. T. Limmer, N. S. Ginsberg, *J. Chem. Phys.* **2020**, *152*, 230901.

[38] R. A. Kerner, Z. Xu, B. W. Larson, B. P. Rand, *Joule* **2021**, *5*, 2273.

[39] G. Y. Kim, A. Senocrate, Y.-R. Wang, D. Moia, J. Maier, *Angew. Chem., Int. Ed.* **2021**, *60*, 820.

[40] G. Y. Kim, A. Senocrate, T.-Y. Yang, G. Gregori, M. Grätzel, J. Maier, *Nat. Mater.* **2018**, *17*, 445.

[41] L. A. Frolova, S. Y. Luchkin, Y. Lekina, L. G. Gutsev, S. A. Tsarev, I. S. Zhidkov, E. Z. Kurmaev, Z. X. Shen, K. J. Stevenson, S. M. Aldoshin, P. A. Troshin, *Adv. Energy Mater.* **2021**, *11*, 2002934.

[42] J. H. Noh, S. H. Im, J. H. Heo, T. N. Mandal, S. I. Seok, *Nano Lett.* **2013**, *13*, 1764.

[43] P. Fedeli, F. Gazza, D. Calestani, P. Ferro, T. Besagni, A. Zappettini, G. Calestani, E. Marchi, P. Ceroni, R. Mosca, *J. Phys. Chem. C* **2015**, *119*, 21304.

[44] K. Suchan, A. Merdasa, C. Rehermann, E. L. Unger, I. G. Scheblykin, *J. Lumin.* **2020**, *221*, 117073.

[45] S. J. Yoon, M. Kuno, P. V. Kamat, *ACS Energy Lett.* **2017**, *2*, 1507.

[46] M. B. Johnston, L. M. Herz, *Acc. Chem. Res.* **2016**, *49*, 146.

[47] L. Tian, J. Xue, R. Wang, *Electronics* **2022**, *11*, 700.

[48] C. Eames, J. M. Frost, P. R. F. Barnes, B. C. O'Regan, A. Walsh, M. S. Islam, *Nat. Commun.* **2015**, *6*, 7497.

[49] A. Senocrate, I. Moudrakovski, G. Y. Kim, T.-Y. Yang, G. Gregori, M. Grätzel, J. Maier, *Angew. Chem., Int. Ed. Engl.* **2017**, *56*, 7755.

[50] D. O. Tiede, M. E. Calvo, J. F. Galisteo-López, H. Míguez, *J. Phys. Chem. Lett.* **2020**, *11*, 4911.

[51] Y.-C. Zhao, W.-K. Zhou, X. Zhou, K.-H. Liu, D.-P. Yu, Q. Zhao, *Light: Sci. Appl.* **2017**, *6*, e16243.

[52] Y.-T. Li, L. Ding, J.-Z. Li, J. Kang, D.-H. Li, L. Ren, Z.-Y. Ju, M.-X. Sun, J.-Q. Ma, Y. Tian, G.-Y. Gou, D. Xie, Y. Yang, L.-W. Wang, L.-M. Peng, T.-L. Ren, *ACS Cent. Sci.* **2019**, *5*, 1857.

[53] Y. Yuan, J. Chae, Y. Shao, Q. Wang, Z. Xiao, A. Centrone, J. Huang, *Adv. Energy Mater.* **2015**, *5*, 1500615.

[54] A. Walsh, S. D. Stranks, *ACS Energy Lett.* **2018**, *3*, 1983.

[55] Z. Ni, H. Jiao, C. Fei, H. Gu, S. Xu, Z. Yu, G. Yang, Y. Deng, Q. Jiang, Y. Liu, Y. Yan, J. Huang, *Nat. Energy* **2022**, *7*, 65.

[56] J. Rappich, F. Lang, V. V. Brus, O. Shargaieva, T. Dittrich, N. H. Nickel, *Sol. RRL* **2020**, *4*, 1900216.

[57] M. Anaya, J. F. Galisteo-López, M. E. Calvo, J. P. Espinós, H. Míguez, *J. Phys. Chem. Lett.* **2018**, *9*, 3891.

[58] E. Mosconi, D. Meggiolaro, H. J. Snaith, S. D. Stranks, F. D. Angelis, *Energy Environ. Sci.* **2016**, *9*, 3180.

[59] L. Huang, Z. Ge, X. Zhang, Y. Zhu, *J. Mater. Chem. A* **2021**, *9*, 4379.

[60] Y. Tian, A. Merdasa, E. Unger, M. Abdellah, K. Zheng, S. McKibbin, A. Mikkelsen, T. Pullerits, A. Yartsev, V. Sundström, I. G. Scheblykin, *J. Phys. Chem. Lett.* **2015**, *6*, 4171.

[61] P. Nandi, C. Giri, D. Swain, U. Manju, S. D. Mahanti, D. Topwal, *ACS Appl. Energy Mater.* **2018**, *1*, 3807.

[62] M. Wansleben, C. Zech, C. Streeck, J. Weser, C. Genzel, B. Beckhoff, R. Mainz, *J. Anal. At. Spectrom.* **2019**, *34*, 1497.

[63] H. Nässtrom, P. Becker, J. A. Márquez, O. Shargaieva, R. Mainz, E. Unger, T. Unold, *J. Mater. Chem. A* **2020**, *8*, 22626.

[64] C. Rehermann, A. Merdasa, K. Suchan, V. Schröder, F. Mathies, E. L. Unger, *ACS Appl. Mater. Interfaces* **2020**, *12*, 30343.

[65] I. L. Braly, R. J. Stoddard, A. Rajagopal, A. R. Uhl, J. K. Katahara, A. K.-Y. Jen, H. W. Hillhouse, *ACS Energy Lett.* **2017**, *2*, 1841.

[66] T. Baikie, N. S. Barrow, Y. Fang, P. J. Keenan, P. R. Slater, R. O. Piltz, M. Gutmann, S. G. Mhaisalkar, T. J. White, *J. Mater. Chem. A* **2015**, *3*, 9298.

[67] Z. Xiao, L. Zhao, N. L. Tran, Y. L. Lin, S. H. Silver, R. A. Kerner, N. Yao, A. Kahn, G. D. Scholes, B. P. Rand, *Nano Lett.* **2017**, *17*, 6863.